Cu and Fe co-doped Ni porous networks as an active electrocatalyst for hydrogen evolution in alkaline medium

Chidanand Hegde,[‡,†] *Xiaoli Sun,*[#,†] *Khang Ngoc Dinh,*[§,Δ] *Huang Aijian,*[⊥] *Hao Ren,*[Δ] *Bing Li,*[±] *Zhiguo Wang,*[⊥,*] *Qingyu Yan,*[§, Δ,*] *Hua Li*[‡,*]

[‡]Singapore Centre for 3D Printing, Department of Mechanical and Aerospace Engineering, Nanyang Technological University, Singapore 639798.

[#]Department of Energy and Power Engineering, Tsinghua University, Beijing, 100084, China.

[§]Energy Research Institute @ NTU (ERI@N), Interdisciplinary Graduate School, Nanyang Technological University, Singapore 637553, Singapore.

[Δ]Department of Materials Science and Engineering, Nanyang Technological University, Singapore 639798.

[⊥]School of Electronics Science and Engineering, University of Electronic Science and Technology of China, Chengdu, 610054, P.R. China.

[±]Institute of Materials Research and Engineering, A*STAR (Agency for Science, Technology, and Research), 2 Fusionopolis Way Innovis #08-03, Singapore 138634.

ABSTRACT: Highly active catalysts from the earth-abundant metals are essential to materialize the low-cost production of hydrogen through water splitting. Herein, nickel porous networks co-doped with Cu and Fe prepared by thermal reduction of pre-synthesized Cu, Fe co-doped $Ni(OH)_2$ nanowires is reported. The sample consists of highly porous network clusters of ~1 µm with a pore size of 10 nm - 100 nm and comprised of nanoparticles of ~80 nm. Among the various doped compositions, the $NiCu_{0.05}Fe_{0.025}$ exhibits excellent catalytic activity with a low overpotential of 60 mV for hydrogen evolution reaction (HER) in 1 M KOH solution and specific activity of 0.1 mA cm^{-2} at 117 mV overpotential calculated based on the electrochemical active surface area (ECSA). The density functional theory calculations reveal the shift of d-bands of nickel to lower values via co-doping of Cu and Fe, resulting in the lowered hydrogen adsorption energy (ΔG_H = -0.131 eV) which is close to ΔG_H for Pt (-0.09 eV). When $NiCu_{0.05}Fe_{0.025}(OH)_2$ nanowires is used as an oxygen evolution reaction (OER) catalyst and is coupled with $NiCu_{0.05}Fe_{0.025}$ porous networks for overall water splitting, the $NiCu_{0.05}Fe_{0.025}$ || $NiCu_{0.05}Fe_{0.025}(OH)_2$ catalyst couple achieves a current density of 10 mA cm^{-2} at 1.491 V similar to that of Pt/C || RuO_2 couple and offers a negligible loss in the performance when operated at 20 mA cm^{-2} for 30 hours.

KEYWORDS: Water splitting, doping, hydrogen evolution reaction, overpotential, tafel slope, specific activity, density functional theory calculation.

INTRODUCTION

Hydrogen is one of the promising energy carriers which can solve the grave problem of environmental pollution. The energy from renewable sources such as solar, wind, tidal, etc. can be used to produce hydrogen from water by electrolysis. However, water electrolysis is energy-

intensive owing to the high overpotential required to overcome the kinetic energy barrier. Consequently, hydrogen production via electrolysis is more expensive compared to natural gas reforming. Therefore, design and synthesis of earth-abundant and highly active catalysts are vital to apply this technique to commercial application.

Electrolysis of water comprises of two half-reactions: the hydrogen evolution reaction (HER) at the cathode, and the more sluggish oxygen evolution reaction (OER) at the anode. The activity of the catalysts for these half-reactions is pH-dependent. HER is favorable in acid electrolytes in contrast to the OER which is more favorable in basic medium. However, to accomplish compatible integration of the catalysts and for efficient overall water splitting, the coupling of the HER and OER catalysts in a common electrolyte is essential [1]. Lack of stability of catalysts in acidic medium coupled with sluggish OER kinetics causes the acid electrolysis lesser favorable to alkaline electrolysis[2]. Therefore, alkaline electrolysis is a better alternative. Advancements in the past decade have resulted in the synthesis of catalysts other than the noble metal catalysts demonstrating modest stability and activity in the alkaline medium [3]. However, since alkaline electrolysis is not favorable to HER the activity of the reported catalysts is not appealing as in the acidic medium. For instance, even the state of the art Pt/C catalyst has two orders of magnitude lesser activity in the basic medium when compared to its activity in the acidic medium [4]. Many of the active catalysts reported for HER in alkali are constitute expensive and scarce elements like Pt [5], Rh [6], and Ru [2]. Therefore, advancement in the catalyst design, leading to synthesis of active catalysts from the earth-abundant elements with reduced cost can significantly boost the progress in hydrogen production via electrolysis.

In view of this, the fundamental understanding of the reaction mechanism is crucial. HER is a two-electron process which involves adsorption of hydrogen on the catalyst surface. The Gibbs

energy of hydrogen adsorption determines the catalytic activity of the surface which in the case of HER should be near to zero for superior activity [7]. The adsorption energy is solely dependent on the electronic structure of the surface which can be engineered to promote reaction pathways with lower energy barriers by doping of suitable elements [8]. Doping of more than one element has been demonstrated to be effective in tuning the adsorption energies of catalysts for HER [5a, 6]. Furthermore, the efficiency of the catalyst depends on both the quantity of the active sites and the efficiency of the single active site [9]. Therefore, the choice of dopants and the concentration of the dopants will play a decisive role in designing a bifunctional catalyst.

In this context, Ni is one of the suitable metals among the earth-abundant elements to be a host for doping owing to its energy of hydrogen adsorption ($\Delta G \approx -0.28$ eV) [10] on (111) plane. By doping elements with positive hydrogen adsorption energies, the ΔG_H for nickel could be tuned to be near zero which is ideal for hydrogen evolution catalyst. Further, computational studies by Greeley *et al*. suggest the plausible boost in the HER performance of nickel by doping of atoms with positive adsorption energies such as copper, silver, and bismuth [7]. Also, NiFe based catalysts have been reported to exhibit high activity towards hydrogen evolution [11]. Inspired by these findings, we chose earth-abundant copper and iron as dopants to tune the catalytic activity of nickel. Cu, Fe co-doped $Ni(OH)_2$ nanowires were synthesized by the hydrothermal process in the first step followed by thermal reduction in hydrogen gas to form Cu, Fe co-doped nickel porous networks. The sample consists of highly porous clusters of ~ 1 µm with pore size of 10 nm - 100 nm and comprises nanoparticles of about 80 nm. The doping concentration of Cu and Fe were varied to optimize HER activity. The $NiCu_{0.05}Fe_{0.025}$ porous networks (hereafter referred as $NiCu_{0.05}Fe_{0.025}$ PNW) with 2.5% doping of Fe and 5% of Cu showed the best performance by achieving a current density of 10 mA cm^{-2} at 60 mV for HER with a Tafel slope of 60.8 mV dec^{-1}

in 1 M KOH solution and exhibited high specific activity of 0.1 mA $cm^{-2}_{(ECSA)}$ at 117 mV overpotential. The density functional theory calculations reveal the shift of d-bands of nickel to lower energy levels resulting in the lowered hydrogen adsorption energy (ΔG_H = -0.131 eV) which is close to ΔG_H for Pt (-0.09 eV), achieved via co-doping of Fe and Cu into Ni lattice, thus promoting enhanced hydrogen evolution. Thus, enhancement of HER activity of Nickel via co-doping of Cu and Fe is demonstrated by experiments and theoretical calculations. When operated at 10 mA cm^{-2} for 20 hours the catalyst displayed negligible loss in the performance revealing excellent stability. Further, the precursor $NiCu_{0.05}Fe_{0.025}(OH)_2$ nanowires exhibit reasonable oxygen evolution reaction (OER) activity with overpotential of 270 mV at 10 mA cm^{-2}. When $NiCu_{0.05}Fe_{0.025}(OH)_2$ is used as an OER catalyst and coupled with $NiCu_{0.05}Fe_{0.025}$ PNW for overall water splitting the $NiCu_{0.05}Fe_{0.025}$ || $NiCu_{0.05}Fe_{0.025}(OH)_2$ cell reaches current density of 10 mA cm^{-2} at 1.491 V outperforming Pt/C || RuO_2 couple and offers modest stability when operated at 20 mA cm^{-2} for 30 hours. This work demonstrates synthesis of active electrocatalysts for water splitting from earth-abundant elements by multi-element doping.

EXPERIMENTAL SECTION

Chemicals. Nickel (II) sulphate hexahydrate ($NiSO_4.6H_2O$, Sigma Aldrich), Copper (II) sulphate pentahydrate ($CuSO_4.5H_2O$, Sigma Aldrich), iron (III) nitrate nonahydrate ($Fe(NO_3)_3.9H_2O$), Urea (NH_2CONH_2, Sigma Aldrich), Pt/C 20% wt. (Fuel cell research) and Nafion (5% solution, Sigma Aldrich) were used without further treatment.

Synthesis of Cu, Fe co-doped $Ni(OH)_2$ nanowires. Cu, Fe co-doped $Ni(OH)_2$ nanowires were synthesized by typical hydrothermal method. 2 mmol of $NiSO_4.6H_2O$ was dissolved in 30 ml DI water. Later $CuSO_4.5H_2O$ and $Fe(NO_3)_3.9H_2O$ were added corresponding to the doping

concentration of Cu and Fe. To the above solution 10 mmol of urea was added and dissolved under magnetic stirring for 15 minutes. The solution was transferred to a 45 ml stainless-steel Teflon-lined autoclave and heated in an electric oven at 120 ^{0}C for 12 hours. After the oven cooled down to room temperature the samples were washed with distilled water and ethanol 3 times and dried in oven at 60 ^{0}C for 12 hours.

Synthesis of Cu, Fe co-doped Ni PNW. Cu, Fe co-doped $Ni(OH)_2$ nanowires powder was transferred to an alumina boat and annealed in a tube furnace with hydrogen gas. The thermal reduction of hydroxides was done at 400 ^{0}C for 2 hours with a ramping rate of 3 ^{0}C per minute.

Sample Characterization. The phase of the synthesized samples was determined using Shimadzu XRD-6000 with Cu-K_α radiation (λ = 1.5406 Å) operated at 40 kV and 30 mA. The synthesized samples were dispersed in ethanol and was drop-cast on a glass slide and used for the measurement. JEOL field emission scanning electron microscope (JSM-7600F, JEOL Ltd. Tokyo, Japan) was used to image the nanostructures formed during the synthesis and for energy-dispersive X-ray spectroscopy (EDX) analysis. High-resolution imaging, elemental mapping, EDX analysis, and high angle annular dark-field scanning transmission electron microscopy (HAADF-STEM) were performed by TEM (JEOL JEM 2100, 200 kV). The surface composition of the samples was studied by X-ray photoelectron spectroscopy from Theta Probe electron spectrometer. The composition of the sample was estimated using Inductive coupled plasma - optical emission spectrometer (PerkinElmer Optima 8000) in which average of three measurements was considered for estimation of concentration of each element.

Electrochemical measurements. The electrochemical measurements were done using Solartron analytical equipment (Model1470E). For the powder samples, 5 mg of powder was dispersed in 950 ul of isopropanol (IPA) and 50 µl of Nafion solution and ultra-sonicated for 1 hour. 5-40 µl of this uniform dispersed slurry was drop cast on a glassy carbon electrode (GCE-3mm) and allowed to dry. The tests for HER performance were conducted using a typical 3 electrode system with Hg/HgO as the reference electrode and Pt mesh as the counter electrode for OER, carbon electrode as counter electrode for HER, and 1 M KOH as the electrolyte. The HER performance was measured by linear sweep voltammetry (LSV) from -0.7 V to -1.7 V vs Hg/HgO at 2 mV per second, and OER performance was measured from 0 V to 1 V vs the reference electrode at 1 mV per second. The measured potential was converted to potential vs. reversible hydrogen electrode (RHE) by using the relation $E_{vsRHE} = E_{vsHg/HgO} + 0.098 + 0.059*$ pH. The durability tests were carried out by chronopotentiometry test by applying a constant current density of 20 mA cm^{-2} for 30 hours and measuring the voltage during the process for overall water splitting and applying constant current density of 10 mA cm^{-2} for 20 hours for HER. For XRD and SEM characterization of post-stability test samples, the catalyst slurry was coated on carbon cloth and chronopotentiometry test was repeated as described above. To estimate the electrochemical active surface area (ECSA) of the samples, cyclic voltammetry (CV) scans were performed between 0.674 V to 0.774 V vs. reference hydrogen electrode at various scan rates from 2 mV/s to 12 mV/s (Supporting Information Figure S5a-b). The difference between the current densities at 0.724 V during the forward and reverse scan ($j_{anodic} - j_{cathodic}$) was plotted against the scan rate. The slope of the plot equals twice the double layer capacitance (Supporting Information Figure S5c) C_{dl}. The roughness factor was calculated by dividing the C_{dl} by the specific capacitance (40 uF cm^{-2}) which was later used for ECSA

normalization [12]. EIS measurements were done in Autolab PGSTAT302 (Eco Chemie, Netherlands) potentiostat by varying the frequency from 100 kHz to 0.1 Hz with an amplitude of 10 mV. The solution resistance Rs was estimated from the x-intercept of the plot of -Z" vs Z' in the high-frequency range which was later used for the iR correction.

Computational methods.

All the calculations were adopted by density functional theory (DFT) methods and implemented in the Vienna Ab initio Simulation Package (VASP)[13] code. The electron-ion interaction was described by using projector augmented wave (PAW) method[14]. And the exchange-correlation was calculated by the generalized gradient approximation (GGA) functional as parametrized by Perdew-Burke-Ernzerhof (PBE), while a 400 eV cutoff energy for plane-wave basis set was used for valence electrons calculation. Self-consistent field (SCF) calculations were performed with the force convergence criterion and energy of 0.02 eV $Å^{-1}$ and10^{-6} eV, respectively. The Brillouin zone was sampled by using a 6×6×1 Monkhorst-Pack k-point mesh in the structure optimization. Moreover, to avoid the interactions between two adjacent periodic structures along the direction perpendicular, a vacuum thickness was selected to be 20 Å. In all cases, spin-polarized considerations were taken into account.

The Gibbs free energy (ΔG_H) of hydrogen atoms adsorption on metal-doped Ni (111) surfaces was calculated by:

$$\Delta G_H = \Delta E_{nH} + \Delta E_{ZPE} - T\Delta S_H \quad (1)$$

the ΔE_{ZPE} and ΔS_H are difference in zero-point energy and entropy between the gas phase and adsorbed state, respectively. ΔE_{nH} is the chemisorption energy of the *n*th H atoms, which was given by:

$$\Delta E_{\mathrm{nH}} = E_{\mathrm{M+nH}} - E_{\mathrm{M+(n-1)H}} - \frac{1}{2}E_{\mathrm{H_2}} \quad (2)$$

where $E_{\mathrm{M+nH}}$ and $E_{\mathrm{M+(n-1)H}}$ are the total energy of metal-doped Ni (111) surfaces with n^{th} and $(n-1)^{th}$ H atoms adsorption. And E_{H2} is the total energy of molecule hydrogen in the gas phase. The calculated frequencies of H_2 gas are 4345 cm^{-1},58 cm^{-1}, and 42 cm^{-1}, which agrees well with previous studies [15]. While the ΔZPE is calculated to be 0.04 eV for H atom adsorption on Ni (111) surfaces, which do not differ notably with the adsorption sites and the doping of different metal atoms. The hydrogen adsorption entropy can be written as $\Delta S_H = \frac{1}{2}S_{H2}$, in which S_{H2} is the entropy of hydrogen molecule in the gas phase at temperature of 300 K under a pressure of 1 bar [16]. In conclusion, the value of ΔE_{ZPE}-$T\Delta S_H$ is equal to 0.245 eV.

RESULTS AND DISCUSSION

Characterization of Cu, Fe co-doped Ni porous nanoclusters.

The hydrothermal process was used to synthesize Cu, Fe doped $Ni(OH)_2$ nanowires. In a typical synthesis, nickel (II) sulfate, copper (II) sulfate and iron (III) nitrate were dissolved in DI water along with urea. The molar ratio of Ni: Cu: Fe was varied to study the effect of doping concentration on catalytic performance. The solution was hydrothermally treated at 120 ^{0}C for 12 hours. The synthesized hydroxide nanowires were annealed in hydrogen furnace at 400 ^{0}C to transform to porous networks (see Experimental Section for details).

To study the effect of doping of Cu and Fe separately on activity for HER, a series of samples were synthesized with varying doping compositions. Firstly, the Cu doping concentration was varied from 1% to 10% to find the optimum doping concentration. Later, the Cu doping concentration was fixed at 5% and Fe doping concentration was varied from 1% to 5%. X-ray

diffraction measurements were carried to investigate the phase and crystallinity of the synthesized powder. The diffraction peaks of all the samples as shown in Figure 1a and Supporting Information Figure S1a-b, located at 44.48^0, 51.83^0 and 76.35^0 are assigned to (111), (200) and (220) planes of nickel (PDF no. #040032941). Identical peaks in all the samples reveal the homogeneous distribution of dopant atoms (Cu and Fe) in the nickel lattice. The inductive couple plasma-atomic emission spectroscopy studies on the $NiCu_{0.05}Fe_{0.025}$ PNW sample confirms the formation of alloy with composition very close to the expected composition from synthesis as shown in Supporting Information Table S1. X-ray photoelectron spectroscopy (XPS) studies were carried out to investigate the surface chemical composition and the chemical states of the constituent elements for the $NiCu_{0.05}Fe_{0.025}$ PNW. XPS survey spectrum (Supporting Information Figure S2) reveals characteristic peaks corresponding to Ni, Cu, Fe, and oxygen. The core-level XPS spectra of Ni 2p, Cu 2p, and Fe 2p are shown in Figure 1b-d. For Ni 2p spectrum two distinct sets of peaks can be observed corresponding to distinct oxidation states of nickel. The peaks at 852.6 eV and 870.3 eV correspond to Ni (0) oxidation state [17]. The Ni $2p_{3/2}$ peak at 855.7 eV along with Ni $2p_{1/2}$ peak at 873.3 eV with spin-orbit splitting energy of 17.6 eV and characteristic satellite peaks at 861.2 eV and 879.8 eV indicate Ni^{2+} oxidation state [18]. Similarly, peaks at 932.7 eV and 952.3 eV in the Cu 2p spectrum correspond to Cu (0) oxidation state. The smaller peaks at 934.6 eV and 954.5 eV along with satellite peaks at 941.3 eV and 944.3 eV indicate the existence of Cu^{2+} [19]. Furthermore, Fe 2p spectrum reveals small peak at 706.8 eV corresponding to Fe (0) state [17] and larger peaks at 711.6 eV and 724.3 eV confirm the presence of oxidized Fe species. Thus, the surface composition of the catalyst reveals the partial oxidation of the metallic surface and confirms the presence of all the three metals Ni, Fe, and Cu on the catalyst surface.

The morphology of the synthesized samples was studied using Field emission scanning electron microscopy (FESEM). The FESEM images of Cu, Fe co-doped $Ni(OH)_2$ reveals the formation of thin nanowires as depicted in Supporting Information Figure S4. After the reduction in the tube furnace with hydrogen flow, the nanowires are transformed to highly porous network clusters of ~ 1 μm comprising numerous nanoparticles of ~ 80 nm as shown in Figure 2a-b and Supporting Information Figure S3a-b. The transmission electron microscope (TEM) images shown in Figure 2c and Supporting Information Figure S3c illustrate the porous network morphology with abundant pores throughout the structure with the dimensions between 10 nm and 100 nm. The porous network morphology is suitable for catalytic activity owing to high surface area and enhanced diffusion of electrolyte for better charge transfer and greater exposure of active sites.

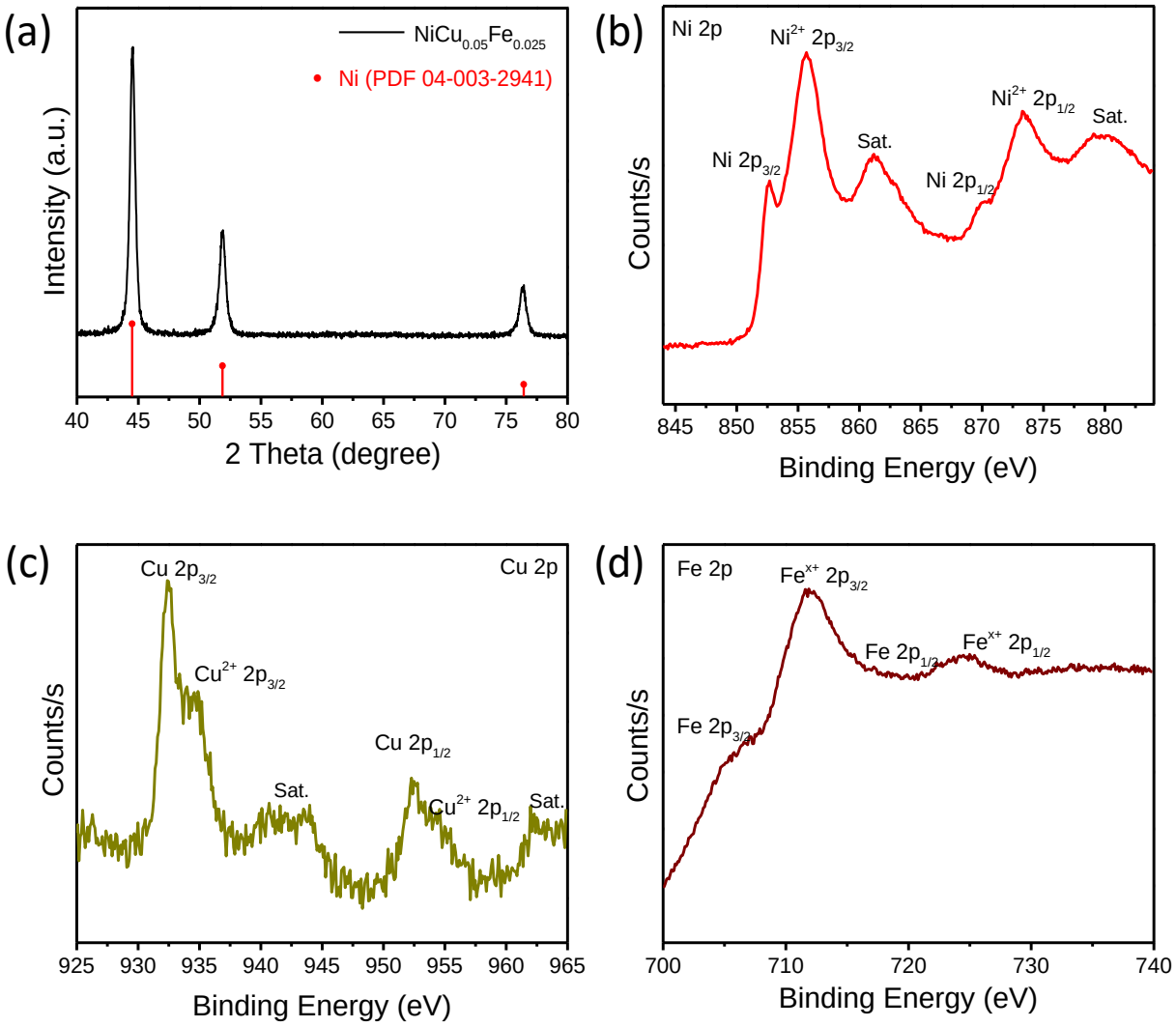

Figure 1. (a) XRD spectrum of $NiCu_{0.05}Fe_{0.025}$ PNW, High resolution XPS spectrum of $NiCu_{0.05}Fe_{0.025}$ PNW in (b) Ni 2p region, (c) Cu 2p region and (d) Fe 2p region.

The high-resolution transmission electron microscope (HRTEM) image (Figure 2d) for the $NiCu_{0.05}Fe_{0.025}$ PNW reveal interplanar spacing of 0.203 nm corresponding to the exposed (111) plane of nickel (PDF no. #040032941). Further, the selected area electron diffraction pattern (SAED) reveals polycrystalline nature of the material with multiple bright spots and rings corresponding to (111), (200) and (220) planes of Ni (Supporting Information Figure S2b).

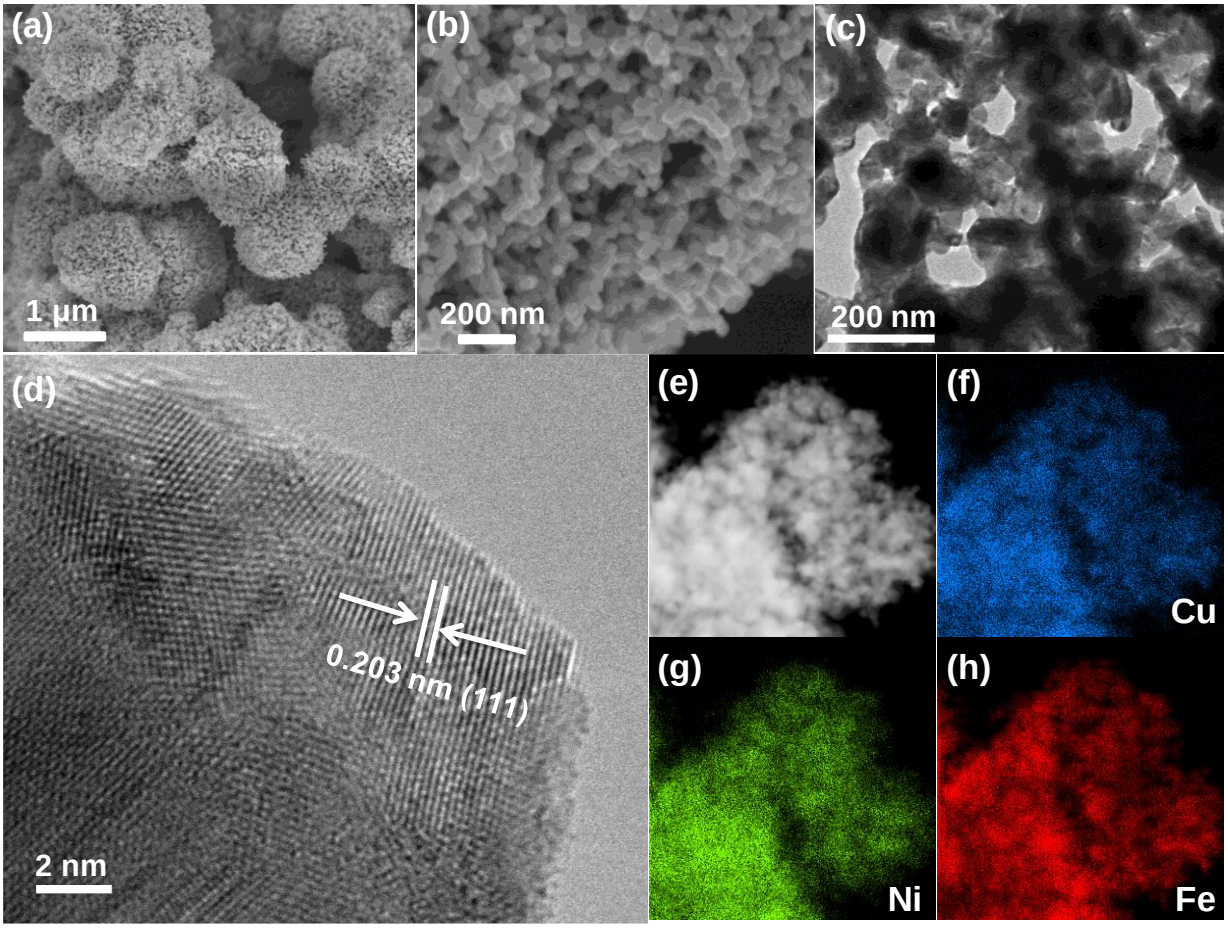

Figure 2. Field emission scanning electron microscopy images of (a-b) $NiCu_{0.05}Fe_{0.025}$ PNW, (c) transmission electron microscopy image, (d) HRTEM image and (e) HAADF-STEM image and (f-h) corresponding STEM-EDX elemental mapping images of $NiCu_{0.05}Fe_{0.025}$ PNW.

The high angle annular dark-field (HAADF) image and corresponding scanning transmission electron microscope energy dispersive X-ray spectroscopy (STEM-EDX) elemental mapping images as shown in Figure 2e-h confirm the homogeneous distribution of Ni, Fe and Cu atoms throughout the nanocluster.

Optimization of the doping composition and catalytic activity of $NiCu_{0.05}Fe_{0.025}$ PNW.

To investigate the effect of Cu doping concentration on the performance of catalyst for hydrogen evolution reaction (HER), four different samples were synthesized with Cu doping concentrations of 1%, 2%, 5%, and 10%. The catalytic performance was measured in 1 M KOH

solution in a typical three-electrode cell with Hg/HgO as the reference electrode and graphite counter electrode and catalyst loaded glassy carbon electrode as the working electrode. To minimize the capacitive current during the tests, a low scan rate of 2 mVs^{-1} was used. . To investigate the effect of mass loading on the catalytic performance the variation of overpotential at 10 mA cm^{-2} was measured. All the overpotentials reported here are with respect to reference hydrogen electrode. Supporting Information Figure S5 illustrates the variation of overpotential for HER with mass loading for Ni PNW, $NiCu_{0.05}Fe_{0.025}$ PNW, and Pt/C catalysts. Based on the results the mass loading corresponding to the saturation region in the plot was used for further studies viz. 1.8 mg cm^{-2} for Cu, Fe co-doped Ni PNW, 2.4 mg cm^{-2} for Ni PNW, and 0.4 mg cm^{-2} for Pt/C catalyst.

Supporting Information Figure S6a depicts the linear sweep voltammetry (LSV) curves for HER with iR correction. The catalysts with 1% ($NiCu_{0.01}$) and 2% ($NiCu_{0.02}$) Cu doping concentrations reach current density of 10 mA cm^{-2} at overpotentials of 90 mV and 86 mV, respectively, exhibiting enhanced activity compared to the pristine nickel PNW which has high overpotential of 123 mV and Tafel slope of 137.45 mV dec^{-1} (Figure 3a-b). On further increasing the doping to 5% ($NiCu_{0.05}$), active HER catalyst is obtained with a low overpotential of 74 mV and Tafel slope of 61.8 mV dec^{-1} (Figure 3a-b). However, further increasing the doping concentration to 10% ($NiCu_{0.1}$) does not improve the HER activity, as seen from the increased overpotential of 87 mV at 10 mA cm^{-2} (Supporting Information Figure S6a). The results indicate a positive improvement in the HER performance with Cu doping concentration up to 5% (Supporting Information Figure S6b). Further, to investigate the effect of Fe doping on the catalytic activity Cu doping concentration was fixed at 5%, while the Fe doping concentration was varied from 1% to 5%. The HER LSV curves depicted in Supporting Information Figure S6c reveal that

$NiCu_{0.05}Fe_{0.01}$ (1% Fe doping) and $NiCu_{0.05}Fe_{0.025}$ (2.5% Fe doping) catalysts show excellent HER activity with low overpotentials of 70 mV and 60 mV at 10 mA cm^{-2}, respectively. However, on the further increase of Fe doping concentration, the HER performance is slightly reduced indicating no positive improvement, as revealed from the higher overpotential of 84 mV for $NiCu_{0.05}Fe_{0.05}$ PNW. Thus, among the Cu, Fe co-doped PNW, $NiCu_{0.05}Fe_{0.025}$ PNW exhibits the best HER activity with a low overpotential of 60 mV@10 mA cm^{-2} and Tafel slope of 60.8 mV dec^{-1} outperforming both pristine Ni PNW and Cu-doped PNW (Figure 3a-b). The activity of the $NiCu_{0.05}Fe_{0.025}$ PNW is slightly inferior to that of Pt/C (20% wt. loading) catalyst, which reaches 10 mA cm^{-2} at a low overpotential of 30 mV and Tafel slope of 32 mV dec^{-1}. A modest Tafel slope of 60.6 mV dec^{-1} indicates the Volmer reaction as the rate-determining step ($E_{cat} + H_2O \rightarrow E_{cat}H_{ads} + OH^-$). The electron impedance spectroscopy (EIS) plots (Figure 3c) also reveal large charge transfer resistance for Ni PNW, which in contrast is significantly lower in the doped samples. This further indicates the enhanced charge transfer kinetics achieved through doping. The $NiCu_{0.05}Fe_{0.025}$ PNW reaches high current density of 100 mA cm^{-2} at a low overpotential of 130 mV surpassing the activity of the noble metal Pt/C (20% wt.) catalyst revealing good mass transfer kinetics at higher potentials. The activity of $NiCu_{0.05}Fe_{0.025}$ PNW is impressive when compared to recently reported earth-abundant catalysts as observed from Supporting Information Table S4. Furthermore, $NiCu_{0.05}Fe_{0.025}$ PNW exhibits negligible loss in performance when operated at a constant current density of 10 mA cm^{-2} for 20 hours (Figure 3d) revealing excellent stability of the catalyst. The FESEM image (Supporting Information Figure S10) of the catalyst after the chronopotentiometry test reveals that the porous network morphology is preserved even after long term electrocatalysis. Further, the phase of the catalyst as observed from the XRD pattern (Supporting Information Figure S9) after the chronopotentiometry test remained same as

the synthesized sample.

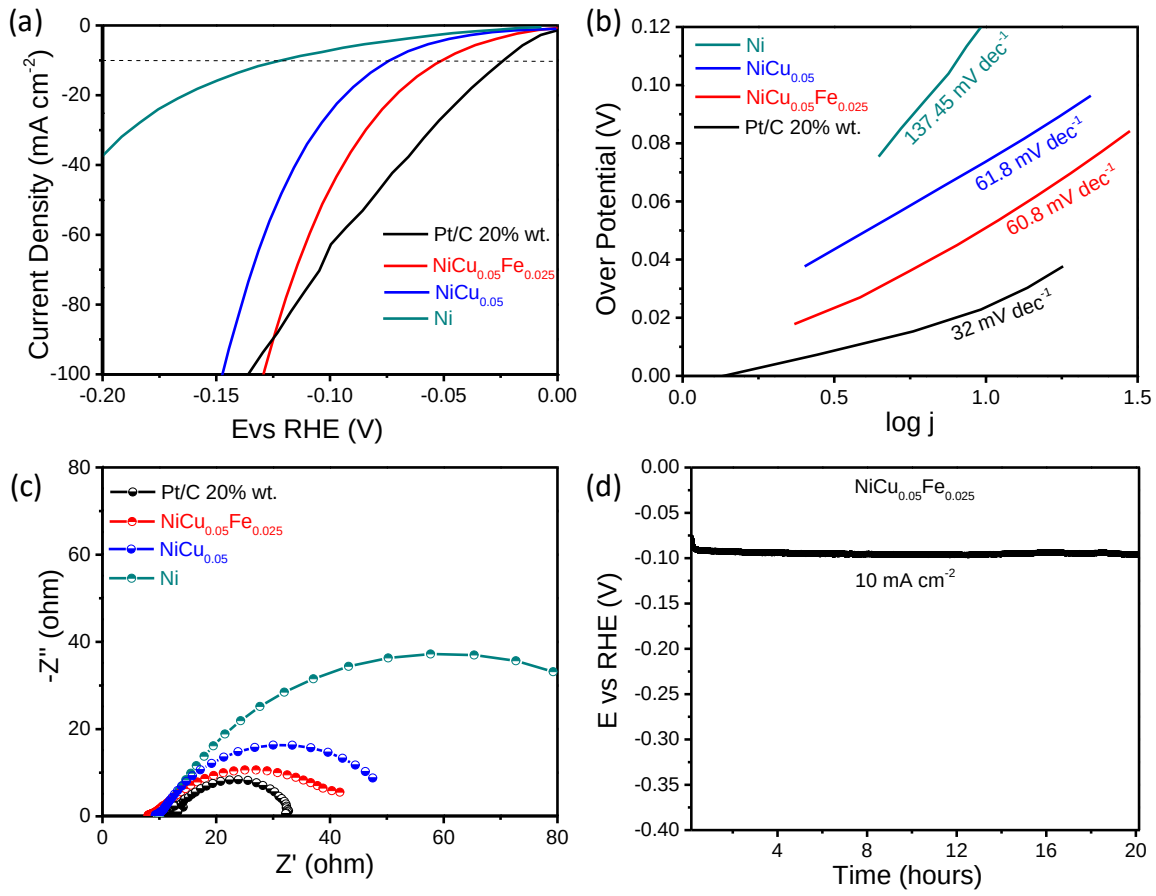

Figure 3. (a) HER polarization curves for $NiCu_{0.05}Fe_{0.025}$ PNW, $NiCu_{0.05}$ PNW, Ni PNW and Pt/C catalysts in 1 M KOH solution and their corresponding (*b*) Tafel slopes, (*c*) EIS plots at -1 V vs Hg/HgO, (*d*) Chronopotentiometry test at constant current density of 10 mA cm^{-2} for 20 hours.

To get further insight into the origin of activity the catalyst, the specific activity of the pristine Ni PNW and $NiCu_{0.05}Fe_{0.025}$ PNW were estimated by computing the normalized current density with respect to the electrochemical active surface area (ECSA) of the catalysts. The ECSA was estimated from the cyclic voltammetry (see Experimental section for details). The plot of ECSA normalized current vs overpotential is illustrated in Supporting Information Figure S8. The

$NiCu_{0.05}Fe_{0.025}$ PNW shows high specific activity of 0.1 mA $cm^{-2}_{(ECSA)}$ at a very low overpotential of 117 mV whereas the Ni PNW requires overpotential of 220 mV to reach the same activity. Interestingly, the double-layer capacitance (C_{dl}) of 23.55 mF cm^{-2} for $NiCu_{0.05}Fe_{0.025}$ PNW is only slightly larger than C_{dl} of 20.35 mF cm^{-2} for Ni PNW (Supporting Information Figure S7c) revealing a minimal increase in the electrochemical active surface area by doping. Thus, we can conclude that the improvement in the catalytic activity of the doped $NiCu_{0.05}Fe_{0.025}$ PNW is primarily due to enhanced intrinsic activity of the active sites achieved via co-doping of Cu and Fe.

Density functional theory calculation.

To investigate the intrinsic properties and determine the active sites of pristine Ni nanosheets and after metal doping, the density functional theory (DFT) calculation was conducted first. Ni belongs to face-centered-cubic (fcc) structures, which contains four Ni atoms in one bulk unit cell as shown in Supporting Information Figure S11a. The lattice constants are a=b=c=3.51 Å with the initial band length d_{Ni-Ni} are 2.48 Å, the result are in a good agreement with experimental data and other theoretical works [20]. In this study, the Ni (111)-surface was selected to investigate HER performance. Because it has been demonstrated highest stability among the low-index surfaces of most fcc metals in previous DFT studies [21]. The top view and side view of optimized Ni-(111) nanosheet with a thickness of ~12 Å are shown in Figure 11b-c, respectively. To determine the catalytic active sites on Ni-(111) nanosheet, different adsorption sites on the surface were considered, in which the most energetically preferable adsorption sites will be selected to describe the HER reactions. Owing to its surface geometry symmetry, there are three possible adsorption sites: top of Ni (S1), the Ni fcc hollow sites (S2), and Ni hcp hollow sites (S3). The favorable adsorption sites for H adsorbates are determined by the adsorption energy ΔE. The calculated ΔE of the fcc hollow sites (-0.50 eV) and hcp hollow sites (-0.49 eV) are

negative than top Ni sites (0.08 eV) as listed in Supporting Information Table S2, proving that the hollow sites (including fcc and hcp hollows) are more thermodynamically preferred for hydrogen adsorption. Additionally, the sites on the bridge between two top Ni atoms are also considered but are found to quickly physically adsorb to the top of Ni sites (S1). This results are agree with previous DFT studies [22].

According to thermodynamics, the Gibbs free energy (ΔG_H) for hydrogen adsorption could be a general criterion for HER activity evaluating. For one ideal catalyst, its ΔG_H should be close to zero. The HER free energy diagram for pristine Ni are illustrated in Figure 4a and also listed in Supporting Information Table S3. The ΔG_H are -0.258 eV for pristine Ni (111) nanosheets, which is not meet the advanced HER catalysts requirement. As we all know, alloying plays an important role in the enhancement of HER performance, Therefore, the Fe-, Cu- and Cu, Fe-doped Ni alloy are also evaluated. As shown in Supporting Information Figure S12, when single metal atoms M (M= Fe or Cu) replace the surface Ni atoms, three types of Ni atoms were examined: top of Ni (S1), Ni fcc sites (S2) and Ni hcp sites (S3). For Cu, Fe co-doped Ni alloy, five possible configurations are considered. The results show that all the single metal atoms prefer to replace the top Ni atoms for their lower total energy and Cu, Fe atoms prefer to replace two top Ni atoms for co-doped Ni alloy formation. The forming energy (E_f) is calculated by:

$$E_f = E_{M\text{-}Ni} - E_{pristine\text{-}Ni} + nE_{Ni} - nE_M \quad (3)$$

where the $E_{M\text{-}Ni}$ and $E_{pristine\text{-}Ni}$ are the total energy of M-doped Ni alloy and pristine Ni nanosheets, respectively; while E_{Ni} and E_M are the energy of individual Ni and M atoms in their stable solid phases; and n means the number of substituted Ni atoms. The calculated formation energies are -0.59 eV, -0.29 eV and -0.84 eV for Fe-, Cu- and Cu, Fe- doped Ni alloy, respectively. The negative values of the forming energy indicate the alloys are energetically

favorable. Cu, Fe co-doped Ni alloy has the lowest forming energy thus demonstrating easier alloy formation.

The HER free energy diagrams for all Ni alloy are illustrated in Figure 4a and listed in Supporting Information Table S3. Due to the change of symmetry of surface geometry, the ΔG_H for six active sites are calculated: top of the doping metal atoms (S1), Ni fcc sites (S2), Ni hcp sites (S3), the top Ni near the doping metal atoms (S4), the amphiposition top Ni atoms (S5 and S6). Similar to pristine Ni nanosheets, the H atoms thermodynamically preferred to adsorb on S2 sites for its lower ΔG_H. The values of ΔG_H increases from -0.258 eV for H adsorbed on pristine Ni nanosheets to -0.208 eV and -0.190 eV for Fe- and Cu- Ni alloy, respectively. The calculated ΔG_H values become closer to the optimum value (0 eV) with the doping of Fe and Cu, which indicates doping of metal atoms can greatly assists the HER performance. Remarkably, the ΔG_H for Cu, Fe co-doped Ni alloy is -0.131 eV, which shows excellent electrocatalytic performance thus better than pristine Ni and other single metal-doped alloy. The result also shows that the doped metal enhances the HER performance of the adjacent regions and not affect the remoter regions, as the ΔG_H for S5 and S6 sites remain ~0.32 eV.

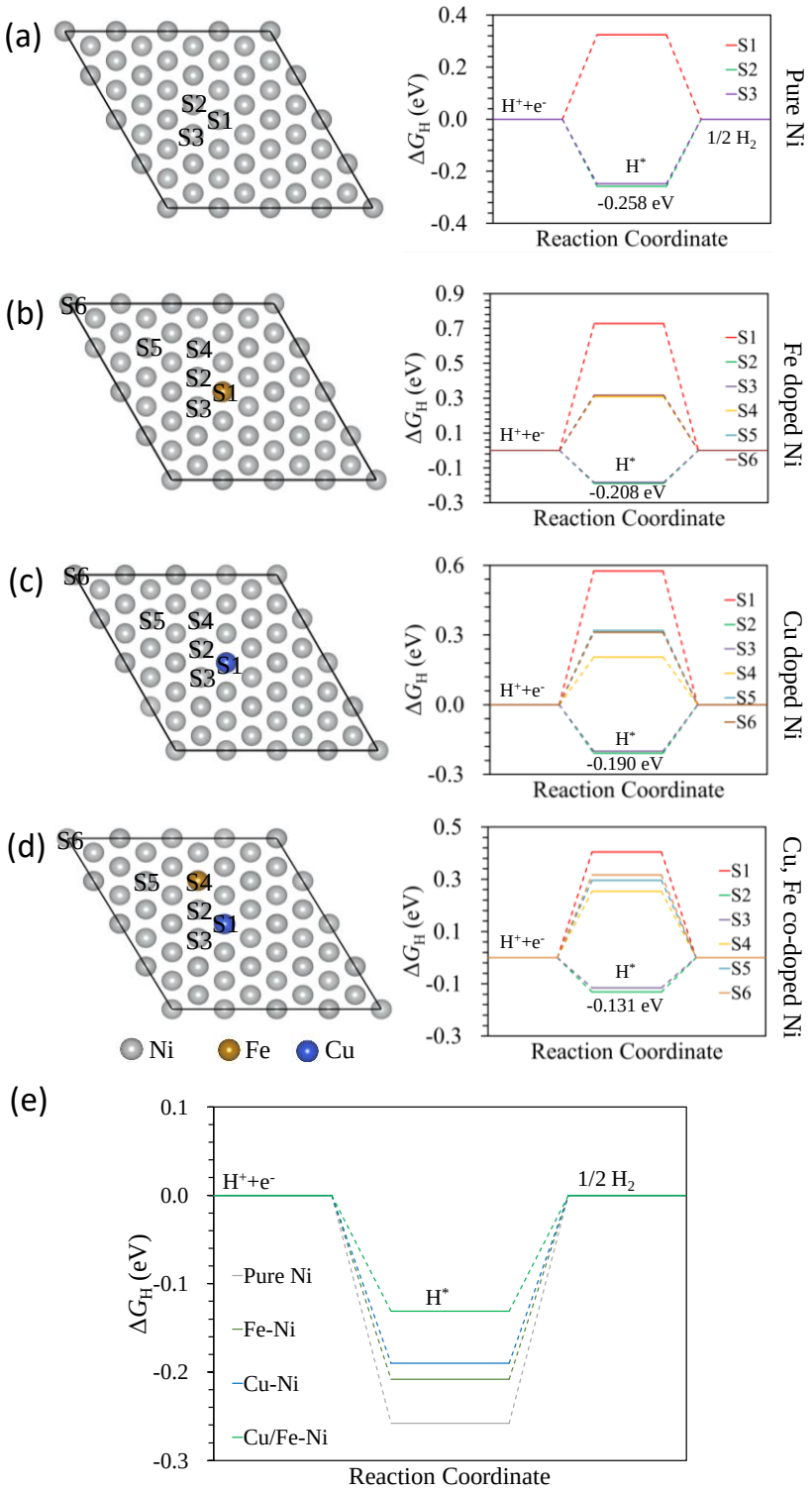

Figure 4. The free energy diagram for H atoms adsorbed on (a) pristine, (b) Fe-, (c) Cu-, (d) Cu, Fe doped Ni nanosheets. The top view and adsorption sites are listed on the left. (e) The Gibbs Free energy for H adsorbed at active site for pristine Ni and Fe-, Cu-, Cu/Fe-doped Ni alloy.

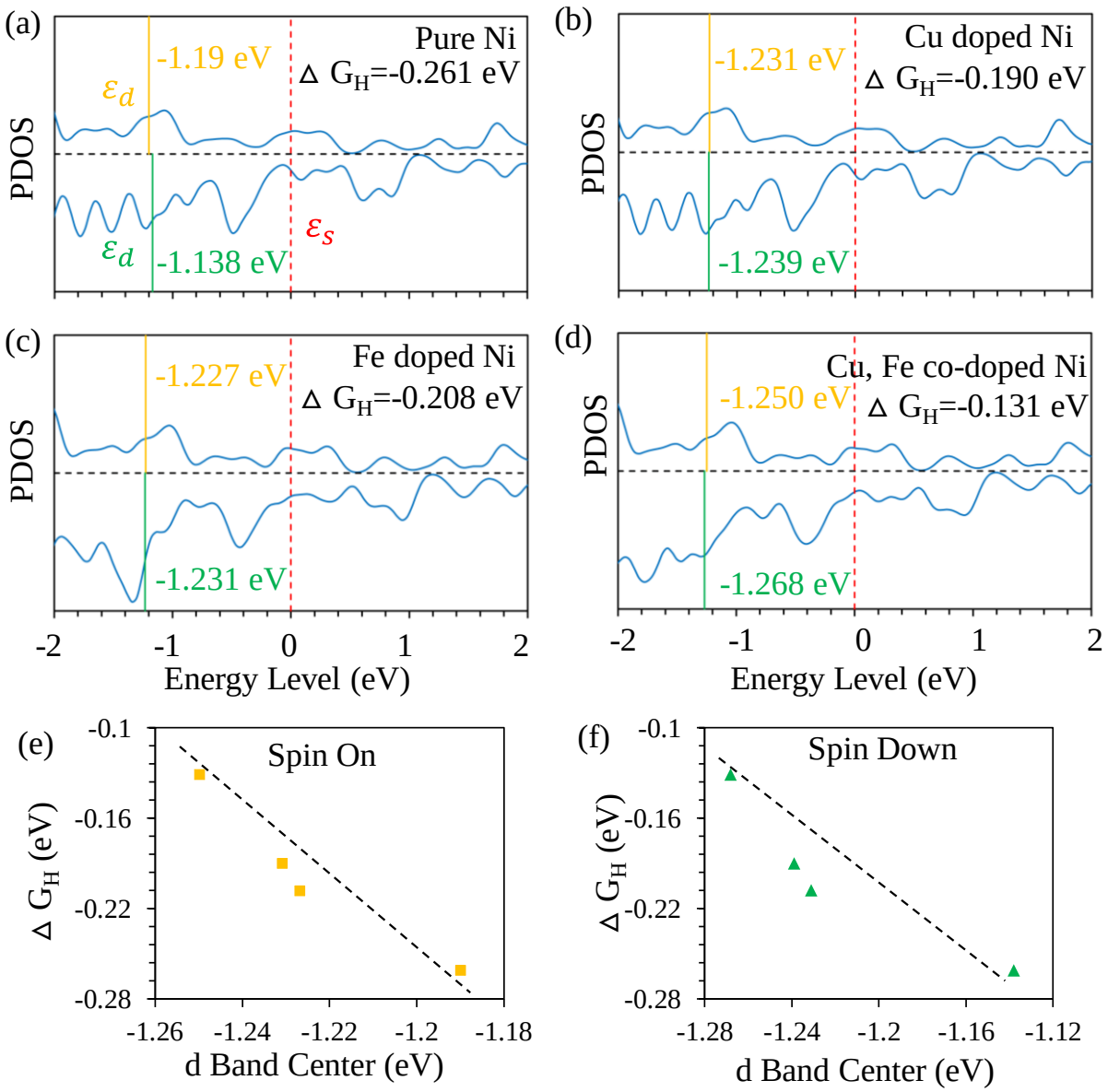

Figure 5. The Projected 3d-orbital density of states of Ni atoms (S2 sites) for (a) pristine, (b) Cu-, (c) Fe-, (d) Cu, Fe- doped Ni nanosheets. The red dotted lines correspond to Ɛs. Spin-polarization was considered as the yellow lines represent the Ɛd for spin on while the green lines show the Ɛd for spin down. (e-f) The relationship between d-band center and Gibbs free energy (ΔG_H) for both spin on and spin down.

According to the *d*-band theory [23], the binding of adsorbates with metals can be determined by the antibonding state occupancy which formed between the valence state of adsorbates and *d*

state of transition metal. Thus, the *d*-band center can be used to indicate the reactivity of metal catalysts from their electronic properties, and the closer the *d*-band center to transition metal *d* state's Fermi energy level, the higher metal reactivity [24]. In this study, for H atoms adsorbed on the Ni nanosheet (111) surface, the Ni atoms 3*d* orbital directly participates in the binding with H atoms. The *d*-band center of pristine and doped Ni nanosheets can be calculated from their projected density of states using the equation (4):

$$\varepsilon_d = \frac{\int_{-\infty}^{+\infty} x\rho(x)dx}{\int_{-\infty}^{+\infty} \rho(x)dx} \tag{4}$$

where, $\rho(x)$ is the PDOS at the energy of x, which is shown in Figure 5a-d. The integral domain was set to be -2 eV to 0 eV of Ni 3*d*-orbital states, representing the closest region near the Fermi energy. And the bonding energy Δε of H atoms on Ni nanosheets can be given by [25]:

$$\Delta\varepsilon \propto -\frac{V^2}{|\varepsilon_d - \varepsilon_s|} \tag{5}$$

V is the coupling matrix element and which can be assumed as a constant value; ε_s is the adsorbate states energy level and can be set to 0 eV. Thus, it can be concluded that the initial bonding energy will increase with the $|\varepsilon_d - \varepsilon_s|$ value decreased.

The calculated ε_d (denoted as yellow lines for spin-on and green lines for spin down) shifts to lower energy levels with the doped of Cu-, Fe- and Cu, Fe-, thus demonstrating a weaker binding of the metal surface with adsorbates. Moreover, a quite clear linear trend of Gibbs free energy (ΔG_H) with ε_d for both spin-on and spin down are shown in Figure 5e-f. It can be also concluded that: (i) the approximately lines present a decrease trendy as *d* band center shift to higher energy level; (ii) the *d* band center are in the range of -1.19 eV to -1.250 eV for spin-on and -1.138 eV to -1.268 eV for spin down, respectively. The similar *d* band center values indicate close ΔG_H values (-0.208 eV to -0.131 eV). (iii) as the pristine Ni nanosheets show stronger adsorption to H

atoms (ΔG_H=-0.258 eV), the a little left shift of ε_d for Cu-, Fe- and Cu, Fe-doped Ni alloy will thus greatly facilitate the simultaneous adsorption of hydrogen, which enhance the HER performance.

Overall water splitting performance:

It is well known that NiFe based hydroxides are active for oxygen evolution in alkaline medium [3a, 26]. Therefore, we investigated the OER performance of precursor $NiCu_{0.05}Fe_{0.025}(OH)_2$ nanowires for the oxygen evolution reaction. The $NiCu_{0.05}Fe_{0025}(OH)_2$ nanowires exhibited reasonable oxygen evolution activity, with overpotential of only 270 mV at 10 mA cm^{-2} (Supporting Information Figure S13). Encouraged by this, the overall water splitting cell was constructed using these two active catalysts. Figure 6a depicts the performance of the synthesized catalysts in comparison with state-of-the-art Pt/C and RuO_2 catalysts. The $NiCu_{0.05}Fe_{0.025}$ || $NiCu_{0.05}Fe_{0.025}(OH)_2$ cell reaches 10 mA cm^{-2} at 1.491 V showing activity similar to that of Pt/C || RuO_2 couple. Furthermore, $NiCu_{0.05}Fe_{0.025}$ || $NiCu_{0.05}Fe_{0.025}(OH)_2$ cell achieves high current density of 100 mA cm^{-2} at extremely low voltage of 1.528 V while the Pt/C || RuO_2 couple requires 1.59 V for the same. In comparison with many of the reported bifunctional catalysts, $NiCu_{0.05}Fe_{0.025}$ || $NiCu_{0.05}Fe_{0.025}(OH)_2$ catalyst couple exhibits excellent overall water splitting performance as seen from the Supporting Information Table S5. Furthermore, chronopotentiometry test at 20 mA cm^{-2} for 30 hours for $NiCu_{0.05}Fe_{0.025}$ || $NiCu_{0.05}Fe_{0.025}(OH)_2$ cell showed minimal loss in activity (Figure 6b) indicating the modest stability of the catalysts for overall water splitting. Since, both HER and OER catalyst in our design contain same elements (Ni, Cu, and Fe) fabrication of electrolyzers can be significantly simplified [27], subsequently reducing the production and maintenance cost required for the commercial application. Thus, through optimized doping of Fe and Cu into Ni, earth-abundant

catalyst couple $NiCu_{0.05}Fe_{0.025}$ || $NiCu_{0.05}Fe_{0.025}(OH)_2$ with a catalyst performance better than the state of the art (Pt/C || RuO_2) catalyst is achieved.

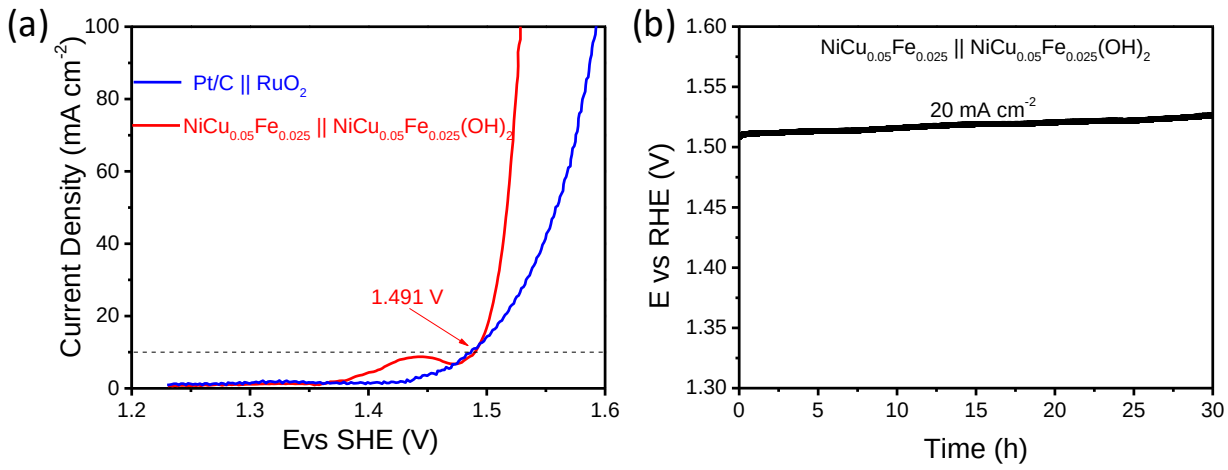

Figure 6. (a) Overall water splitting performance of $NiCu_{0.05}Fe_{0.025}$ || $NiCu_{0.05}Fe_{0.025}(OH)_2$ cell in comparison with Pt/C || RuO_2 cell, (d) Chronopotentiometry test for the overall water splitting by using $NiCu_{0.05}Fe_{0.025}$ || $NiCu_{0.05}Fe_{0.025}(OH)_2$ cell.

CONCLUSIONS

In conclusion, Cu, Fe co-doped Ni PNW is synthesized which exhibits excellent activity for hydrogen evolution in 1 M KOH solution. An investigation into the effect of doping concentration of Cu and Fe reveals that doping concentration of both the elements is critical to catalyst performance. After investigating various doping compositions, we conclude that the catalyst with 5% Cu doping and 2.5% Fe doping exhibits the best HER activity. The HER activity of $NiCu_{0.05}Fe_{0.025}$ PNW is evident from the low overpotential of 60 mV to reach 10 mA cm^{-2} current density at a Tafel slope of 60.8 mV dec^{-1} and excellent stability when operated for 20 hours. Further, the $NiCu_{0.05}Fe_{0.025}$ PNW displays high specific activity of 0.1 mA $cm^{-2}_{(ECSA)}$ at a low overpotential of 117 mV. The DFT calculations reveal the shift of d-band center to lower values due to co-doping of Fe and Cu. Consequently, the hydrogen adsorption energy of Ni is changed from -0.258 eV in the pristine Ni to -0.131 eV for the Cu, Fe co-doped Ni which is very

close to ΔG_H for Pt (-0.09 eV) [10] leading to optimized hydrogen adsorption suitable for high catalytic activity. When $NiCu_{0.05}Fe_{0.025}(OH)_2$ nanowires is used as OER catalyst and coupled with $NiCu_{0.05}Fe_{0.025}$ PNW for overall water splitting the cell requires only 1.491 V to reach 10 mA cm^{-2} current density and is stable when operated at 20 mA cm^{-2} for 30 hours. In conclusion, this study demonstrates a novel way of catalyst design and synthesis involving more than one dopant atoms to achieve an optimized electronic structure to promote active hydrogen evolution for water splitting.

AUTHOR INFORMATION

Corresponding Authors

*E-mail: (Qingyu Yan) - alexyan@ntu.edu.sg .

(Zhiguo Wang) - zgwang@uestc.edu.cn .

(Hua Li) - lihua@ntu.edu.sg .

Author contributions

†These authors contributed equally to this work.

ACKNOWLEDGEMENTS

The authors thank Singapore Center for 3D Printing for the financial support for this project. We also would like to acknowledge the Facility for Analysis, Characterization, Testing, and Simulation (FACTS), Nanyang Technological University, Singapore, for use of their electron microscopy and XRD facilities.

REFERENCES

1. Jiang, N.; You, B.; Sheng, M.; Sun, Y., Electrodeposited cobalt-phosphorous-derived films as competent bifunctional catalysts for overall water splitting. *Angewandte Chemie* **2015,** *54* (21), 6251-4.

2. Lu, B.; Guo, L.; Wu, F.; Peng, Y.; Lu, J. E.; Smart, T. J.; Wang, N.; Finfrock, Y. Z.; Morris, D.; Zhang, P.; Li, N.; Gao, P.; Ping, Y.; Chen, S., Ruthenium atomically dispersed in carbon outperforms platinum toward hydrogen evolution in alkaline media. *Nat Commun* **2019,** *10* (1), 631.

3. (a) Gong, M.; Li, Y.; Wang, H.; Liang, Y.; Wu, J. Z.; Zhou, J.; Wang, J.; Regier, T.; Wei, F.; Dai, H., An advanced Ni-Fe layered double hydroxide electrocatalyst for water oxidation. *Journal of the American Chemical Society* **2013,** *135* (23), 8452-5; (b) Burke, M. S.; Enman, L. J.; Batchellor, A. S.; Zou, S.; Boettcher, S. W., Oxygen Evolution Reaction Electrocatalysis on Transition Metal Oxides and (Oxy)hydroxides: Activity Trends and Design Principles. *Chemistry of Materials* **2015,** *27* (22), 7549-7558; (c) Lu, F.; Zhou, M.; Zhou, Y.; Zeng, X., First-Row Transition Metal Based Catalysts for the Oxygen Evolution Reaction under Alkaline Conditions: Basic Principles and Recent Advances. *Small* **2017,** *13* (45).

4. Durst, J.; Siebel, A.; Simon, C.; Hasché, F.; Herranz, J.; Gasteiger, H. A., New insights into the electrochemical hydrogen oxidation and evolution reaction mechanism. *Energy Environ. Sci.* **2014,** *7* (7), 2255-2260.

5. (a) Oh, A.; Sa, Y. J.; Hwang, H.; Baik, H.; Kim, J.; Kim, B.; Joo, S. H.; Lee, K., Rational design of Pt-Ni-Co ternary alloy nanoframe crystals as highly efficient catalysts toward the alkaline hydrogen evolution reaction. *Nanoscale* **2016,** *8* (36), 16379-16386; (b) Wang, P.; Jiang, K.; Wang, G.; Yao, J.; Huang, X., Phase and Interface Engineering of Platinum-Nickel Nanowires for Efficient Electrochemical Hydrogen Evolution. *Angewandte Chemie* **2016,** *55* (41), 12859-63; (c) Cheng, Z.; Geng, X.; Chen, L.; Zhang, C.; Huang, H.; Tang, S.; Du, Y., In situ synthesis of chemically ordered primitive cubic Pt3Co nanoparticles by a spray paint drying method for hydrogen evolution reaction. *Journal of Materials Science* **2018,** *53* (17), 12399-12406.

6. Zhang, L.; Lu, J.; Yin, S.; Luo, L.; Jing, S.; Brouzgou, A.; Chen, J.; Shen, P. K.;

Tsiakaras, P., One-pot synthesized boron-doped RhFe alloy with enhanced catalytic performance for hydrogen evolution reaction. *Applied Catalysis B: Environmental* **2018,** *230*, 58-64.

7. Greeley, J.; Jaramillo, T. F.; Bonde, J.; Chorkendorff, I.; Nørskov, J. K., Computational high-throughput screening of electrocatalytic materials for hydrogen evolution. *Nature materials* **2006,** *5* (11), 909-913.

8. Norskov, J. K.; Bligaard, T.; Rossmeisl, J.; Christensen, C. H., Towards the computational design of solid catalysts. *Nature chemistry* **2009,** *1* (1), 37-46.

9. Luo, X.; Shao, Q.; Pi, Y.; Huang, X., Trimetallic Molybdate Nanobelts as Active and Stable Electrocatalysts for the Oxygen Evolution Reaction. *ACS Catalysis* **2018,** *9* (2), 1013-1018.

10. Nørskov, J. K.; Bligaard, T.; Logadottir, A.; Kitchin, J. R.; Chen, J. G.; Pandelov, S.; Stimming, U., Trends in the Exchange Current for Hydrogen Evolution. *Journal of The Electrochemical Society* **2005,** *152* (3), J23.

11. (a) Dinh, K. N.; Zheng, P.; Dai, Z.; Zhang, Y.; Dangol, R.; Zheng, Y.; Li, B.; Zong, Y.; Yan, Q., Ultrathin Porous NiFeV Ternary Layer Hydroxide Nanosheets as a Highly Efficient Bifunctional Electrocatalyst for Overall Water Splitting. *Small* **2017**; (b) Long, X.; Li, G.; Wang, Z.; Zhu, H.; Zhang, T.; Xiao, S.; Guo, W.; Yang, S., Metallic Iron-Nickel Sulfide Ultrathin Nanosheets As a Highly Active Electrocatalyst for Hydrogen Evolution Reaction in Acidic Media. *Journal of the American Chemical Society* **2015,** *137* (37), 11900-3; (c) Yu, J.; Cheng, G.; Luo, W., Ternary nickel–iron sulfide microflowers as a robust electrocatalyst for bifunctional water splitting. *Journal of Materials Chemistry A* **2017,** *5* (30), 15838-15844.

12. McCrory, C. C.; Jung, S.; Peters, J. C.; Jaramillo, T. F., Benchmarking heterogeneous electrocatalysts for the oxygen evolution reaction. *Journal of the American Chemical Society* **2013,** *135* (45), 16977-87.

13. Kresse, G., Efficient iterative schemes for ab initio total-energy calculations using a plane-wave basis set. *PHYSICAL REVIEW B* **1996,** *54*, 11169e11186.

14. Furthmu¨ller, G. K. J., Efficient iterative schemes for ab initio total-energy calculations using a plane-wave basis set. *PHYSICAL REVIEW B* **1999,** *54*, 11169-11186.

15. (a) Chris G. Van de Walle a, Jonathan P. Goss b, Energetics and vibrational frequencies of interstitial H2 molecules

in semiconductors. *Materials Science and Engineering B* **1999,** *58*, 17-23; (b) David M. Bishop,

S. M. C., Calculation of the fundamental vibrational frequencies
and intensities of Hz, D2, and N2 in the presence of Li+ or Na+. *Chemical Physics Letters* **1994,** *230*, 177-181.

16. Voiry, D.; Yamaguchi, H.; Li, J.; Silva, R.; Alves, D. C.; Fujita, T.; Chen, M.; Asefa, T.; Shenoy, V. B.; Eda, G.; Chhowalla, M., Enhanced catalytic activity in strained chemically exfoliated WS(2) nanosheets for hydrogen evolution. *Nature materials* **2013,** *12* (9), 850-5.

17. Changhong Wang, H. Y., Yejun Zhang and Qiangbin Wang, NiFe alloy nanoparticle with HCP structure stimulates superior OER. *Angewandte Chemie International Edition* **2019**.

18. Fan, K.; Chen, H.; Ji, Y.; Huang, H.; Claesson, P. M.; Daniel, Q.; Philippe, B.; Rensmo, H.; Li, F.; Luo, Y.; Sun, L., Nickel-vanadium monolayer double hydroxide for efficient electrochemical water oxidation. *Nature communications* **2016,** *7*, 11981.

19. Jin, Z.; Liu, C.; Qi, K.; Cui, X., Photo-reduced Cu/CuO nanoclusters on TiO2 nanotube arrays as highly efficient and reusable catalyst. *Scientific reports* **2017,** *7*, 39695.

20. (a) Bozzolo, G.; Ferrante, J., Determination of parameters of a method for predicting alloy properties. *Physical Review B* **1992,** *46* (13), 8600-8602; (b) Zarechnaya, E. Y.; Skorodumova, N. V.; Simak, S. I.; Johansson, B.; Isaev, E. I., Theoretical study of linear monoatomic nanowires, dimer and bulk of Cu, Ag, Au, Ni, Pd and Pt. *Computational Materials Science* **2008,** *43* (3), 522-530.

21. Wang, Y. W., W.; Fan, K.-N.; Deng, J., Structural and Electronic Properties of Silver Surfaces: Ab Initio Pseudopotential Density Functional Study. *Surf. Sci.* **2001,** *490*, 125-132.

22. Dong, Y.; Dang, J.; Wang, W.; Yin, S.; Wang, Y., First-Principles Determination of Active Sites of Ni Metal-Based Electrocatalysts for Hydrogen Evolution Reaction. *ACS applied materials & interfaces* **2018,** *10* (46), 39624-39630.

23. Norskov, J. K.; Abild-Pedersen, F.; Studt, F.; Bligaard, T., Density functional theory in surface chemistry and catalysis. *Proc Natl Acad Sci U S A* **2011,** *108* (3), 937-43.

24. Hwang, S. J.; Kim, S.-K.; Lee, J.-G.; Lee, S.-C.; Jang, J. H.; Kim, P.; Lim, T.-H.; Sung, Y.-E.; Yoo, S. J., Role of Electronic Perturbation in Stability and Activity of Pt-Based Alloy Nanocatalysts for Oxygen Reduction. *Journal of the American Chemical Society* **2012,** *134* (48), 19508-19511.

25. (a) Tsai, C.; Chan, K.; Abild-Pedersen, F.; Norskov, J. K., Active edge sites in MoSe2 and WSe2 catalysts for the hydrogen evolution reaction: a density functional study. *Physical*

chemistry chemical physics : PCCP **2014,** *16* (26), 13156-64; (b) Ouyang, Y.; Ling, C.; Chen, Q.; Wang, Z.; Shi, L.; Wang, J., Activating Inert Basal Planes of MoS2 for Hydrogen Evolution Reaction through the Formation of Different Intrinsic Defects. *Chemistry of Materials* **2016,** *28* (12), 4390-4396.

26. Friebel, D.; Louie, M. W.; Bajdich, M.; Sanwald, K. E.; Cai, Y.; Wise, A. M.; Cheng, M. J.; Sokaras, D.; Weng, T. C.; Alonso-Mori, R.; Davis, R. C.; Bargar, J. R.; Norskov, J. K.; Nilsson, A.; Bell, A. T., Identification of highly active Fe sites in (Ni,Fe)OOH for electrocatalytic water splitting. *Journal of the American Chemical Society* **2015,** *137* (3), 1305-13.

27. Xiong, B.; Chen, L.; Shi, J., Anion-Containing Noble-Metal-Free Bifunctional Electrocatalysts for Overall Water Splitting. *ACS Catalysis* **2018**.